nature materials

ARTICLES

https://doi.org/10.1038/s41563-020-0763-z

Direct observation of highly confined phonon polaritons in suspended monolayer hexagonal boron nitride

Ning Li[1,2,3,4,13], Xiangdong Guo[1,4,5,6,13], Xiaoxia Yang[1,5]✉, Ruishi Qi[2], Tianyu Qiao[2], Yifei Li[7], Ruochen Shi[2,3], Yuehui Li[2,3], Kaihui Liu[6,8], Zhi Xu[9], Lei Liu[7], F. Javier García de Abajo[10,11], Qing Dai[1,5]✉, En-Ge Wang[2,8,9,12] and Peng Gao[2,3,4,8]✉

Phonon polaritons enable light confinement at deep subwavelength scales, with potential technological applications, such as subdiffraction imaging, sensing and engineering of spontaneous emission. However, the trade-off between the degree of confinement and the excitation efficiency of phonon polaritons prevents direct observation of these modes in monolayer hexagonal boron nitride (h-BN), where they are expected to reach ultrahigh confinement. Here, we use monochromatic electron energy-loss spectroscopy (about 7.5 meV energy resolution) in a scanning transmission electron microscope to measure phonon polaritons in monolayer h-BN, directly demonstrating the existence of these modes as the phonon Reststrahlen band (RS) disappears. We find phonon polaritons in monolayer h-BN to exhibit high confinement (>487 times smaller wavelength than that of light in free space) and ultraslow group velocity down to about $10^{-5}c$. The large momentum compensation provided by electron beams additionally allows us to excite phonon polaritons over nearly the entire RS band of multilayer h-BN. These results open up a broad range of opportunities for the engineering of metasurfaces and strongly enhanced light–matter interactions.

Hyperbolic phonon polaritons (HPhPs) in two-dimensional (2D) van der Waals materials, such as hexagonal boron nitride (h-BN), can be used to confine and manipulate light at deep subwavelength nanoscales[1–3], where they find important applications in subdiffraction imaging[4,5], surface-enhanced infrared spectroscopy[6–8], nanoscale lasing[3] and integrated optical circuits[1,9], among other applications[10]. HPhPs in monolayer h-BN are expected to reach ultrahigh confinement[11]. Additionally, the Reststrahlen (RS) band in monolayer h-BN disappears at the Γ point, which implies totally different properties from those of HPhPs in multilayer h-BN[12]. However, a quantitative measurement of the pristine HPhPs in monolayer h-BN still remains elusive due to the large light–polariton wave vector mismatch, as well as the effects of the supporting substrate[13–16]. Although a weak HPhP signal in monolayer h-BN supported on SiO_2 substrate was recently reported from a scattering-type scanning near-field optical microscopy (s-SNOM) study[17], the measured HPhP frequency[17] was much lower than the theoretically calculated transverse optical (TO) phonon frequency in free-standing monolayer h-BN[12]. Besides, the corresponding theoretical modelling has encountered difficulties in calculating the optical properties of monolayer h-BN[12]. It is therefore important to detect HPhPs directly in suspended monolayer h-BN to unveil their intrinsic properties.

To excite HPhPs in monolayer h-BN, momentum compensation should be above $10^6\,cm^{-1}$ (refs. [11,12]). While methods based on s-SNOM are widely used to probe 2D polaritons because they have the advantage of high-resolution imaging in real space, the momentum compensation of the s-SNOM typically reaches ~$10^5\,cm^{-1}$, as determined by the size of the tip and the extension of the near field[11,18,19]. Thus, only HPhPs in a narrow frequency window have been measured using these optical methods[4,5,11]. As a complement to optical excitation approaches, fast electrons can transfer much larger momentum than photons[20], therefore holding great potential for the excitation of highly confined 2D polaritons.

Electron energy-loss spectroscopy (EELS) incorporated in a scanning transmission electron microscope (STEM–EELS) equipped with a monochromator and aberration corrector offers combined high spatial[21] and energy[22] resolutions, enabling measurements of lattice vibrations, interband transitions and interactions mediated by large-momenta exchanges in systems ranging from the nano to the atomic scale. For example, the vibrational spectra of SiO_2 and h-BN were studied via STEM–EELS[23], while a polariton-induced shift of the resonance peak of thin h-BN was later probed when the electron beam was placed at different positions[24]. Recently, the longitudinal optical (LO) phonon and the HPhPs were resolved as two split peaks in h-BN thin films[22], and the behaviour of phonon peaks across the Brillouin zone (BZ) was also studied[25]. However, owing to the insufficient energy resolution, these EELS spectra can only qualitatively reflect the existence of propagating phonon polaritons in h-BN, but not quantitatively study the dispersion of the HPhPs in h-BN.

[1]Division of Nanophotonics, CAS Key Laboratory of Standardization and Measurement for Nanotechnology, CAS Center for Excellence in Nanoscience, National Center for Nanoscience and Technology, Beijing, China. [2]International Center for Quantum Materials, Peking University, Beijing, China. [3]Electron Microscopy Laboratory, School of Physics, Peking University, Beijing, China. [4]Academy for Advanced Interdisciplinary Studies, Peking University, Beijing, China. [5]Center of Materials Science and Optoelectronics Engineering, University of Chinese Academy of Sciences, Beijing, China. [6]State Key Laboratory for Mesoscopic Physics, School of Physics, Peking University, Beijing, China. [7]Department of Materials Science and Engineering, College of Engineering, Peking University, Beijing, China. [8]Collaborative Innovation Center of Quantum Matter, Beijing, China. [9]Songshan Lake Materials Laboratory, Institute of Physics, Chinese Academy of Sciences, Dongguan, China. [10]ICFO-Institut de Ciencies Fotoniques, The Barcelona Institute of Science and Technology, Barcelona, Spain. [11]ICREA-Institució Catalana de Recerca i Estudis Avançats, Barcelona, Spain. [12]School of Physics, Liaoning University, Shenyang, China. [13]These authors contributed equally: Ning Li, Xiangdong Guo. ✉e-mail: yangxx@nanoctr.cn; daiq@nanoctr.cn; p-gao@pku.edu.cn

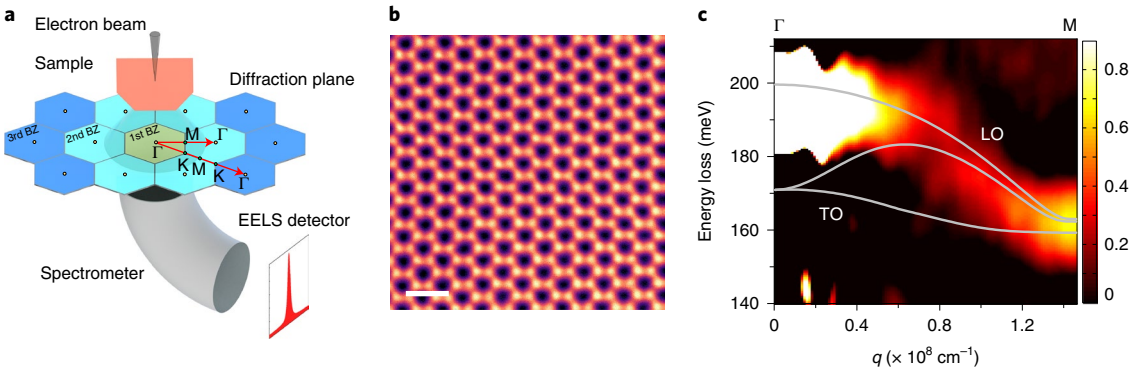

Fig. 1 | Measurement of vibrational spectra of h-BN in a wide momentum range. a, Schematic of electron energy-loss spectroscopy incorporated in a scanning transmission electron microscope. From top to bottom, the electron beam (indicated by the grey cone) is focused on the h-BN sample (the orange thin flake), and the obtained diffraction plane of h-BN is displayed by yellow, light-green and blue hexagons, which correspond to the first- to third-order BZs, respectively. The red arrows indicate Γ–M–Γ and Γ–K–M–K–Γ directions in the reciprocal space of h-BN; the spectrometer is simplified as a curved pipe and an EELS spectrum is presented on the EELS detector. **b**, Atomically resolved HAADF image of a h-BN flake showing the high quality of h-BN and the high spatial resolution at 60 kV (better than 1.07 Å). Scale bar, 0.5 nm. **c**, Phonon dispersion curve of an h-BN flake from Γ to M in momentum space, the colour scale indicates the processed EELS intensity in arbitrary units (details in Methods). The grey curves are the calculated phonon dispersion obtained through density functional theory.

Here, using STEM–EELS with an improved energy resolution down to 7.5 meV, we experimentally measure HPhPs in suspended monolayer h-BN and in sub-10-nm-thick h-BN flakes covering nearly the whole upper RS band. The polariton dispersion can be directly extracted from the EELS spectra, from which we identify a surface HPhP mode in h-BN flakes. We find HPhPs in monolayer h-BN to exhibit ultrahigh confinement (>487 times smaller wavelength relative to the wavelength of light in free space) and ultraslow group velocity (~10^{-5} c). This work experimentally demonstrates the existence of high-quality HPhPs when the RS band disappears in monolayer h-BN, thus providing useful insights for the design of optical integrated circuits and surface-enhanced infrared spectroscopy with enhanced light–matter interactions.

HPhPs in ultrathin h-BN flake

Figure 1a presents the schematic of STEM–EELS in our experiments. By using a fast electron beam, STEM–EELS can supply high momentum compensation for the excitation of phonons or phonon polaritons, covering the whole first and part of the second-order BZs, as indicated in the diffraction plane of h-BN. As shown in Fig. 1b, the high-angle annular dark field (HAADF) image with spatial resolution better than 1.07 Å recorded at 60 kV demonstrates superior quality of the h-BN crystal. Figure 1c shows the as-measured phonon dispersion of the h-BN in the first BZ (details in Methods), which agrees well with first-principles calculations (grey curves). The results demonstrate that an ultrahigh momentum compensation (up to 1.4×10^8 cm^{-1}) can be supplied in the EELS measurements.

In our STEM–EELS measurements, the high-quality h-BN flakes are suspended on lacy carbon TEM grids (Methods). At first, we measure an ~10-nm-thick h-BN nanoflake, whose morphology is shown in the inset of Fig. 2a. The EELS experiments are operated at 60 kV with an energy resolution of ~7.5 meV (see Supplementary Fig. 1). Figure 2a presents two EELS spectra of the h-BN flake acquired in aloof configuration (in vacuum, 10 nm away from a h-BN edge) and bulk geometry (inside the flake, 20 nm away from the edge). In the aloof configuration, only one peak at 173 meV is observed, which is consistent with previous studies[23,24], while the bulk geometry spectrum reveals three peaks at 173 meV, 182 meV and 196 meV, which have not been resolved in previous studies[22–24]. To investigate these three peaks, the EELS spectra of the h-BN flake are spatially mapped by a 2-Å-sized electron beam. Figure 2b shows line profiles recorded as the electron beam is moved from aloof to bulk positions (along the red arrow in the inset of Fig. 2a, with a 9-nm spacing between successive beam spots).

To understand the three modes, we perform finite-element method (FEM) simulations that reproduce the EELS spectra (Fig. 2c, see details in Methods and Supplementary Notes), which are in excellent agreement with experimental spectra. The right peak (brown curve) sits at a constant energy loss of 196 meV, which is between the surface optical phonon (SO, 195 meV) and the LO phonon (200 meV). By comparing the simulated EELS spectra before and after considering the zero-loss peak (ZLP) tail of the electron beam, that is, performing Gaussian convolution by a peak with 7.5 meV full width at half maximum (FWHM), the 200-meV peak redshifts to 196 meV (Fig. 2c and Supplementary Fig. 2a). Thus, the experimentally observed 196-meV peak can be assigned to the LO phonon. Moreover, the strength of this mode is evenly distributed over the h-BN flake, which is a characteristic of the LO phonon. In contrast, the SO phonon is mainly localized at the edge[19,26,27], as demonstrated in the FEM calculation (Supplementary Figs. 2 and 3). We expected to observe the SO phonon at a slightly lower energy ~195 meV. However, it is not observed in our experiments, a fact that we attribute to the combination of strong localization at the boundary (Supplementary Fig. 2a) and imperfections in the edge of the h-BN flake (not sufficiently sharp).

The central peak shifts from ~195 meV to ~183 meV as the electron-beam probe moves from the edge to inside the sample, which is characteristic of phonon polaritons. This change is more clearly visible when we plot the deconvoluted experimental spectra (see details in Methods) in a 2D map as a function of electron beam position (Supplementary Fig. 4). The excited polaritons propagate to, and are reflected by, the edge, and then interfere with the excited polaritons. The maximum in the EELS signal happens at $2q|d|+\phi_{\mathrm{refl}}=2\pi$, where q is the momentum, d is the distance to the edge boundary and ϕ_{refl} is the phase change introduced by the reflection[19,28]. We further extract the dispersion of HPhPs in h-BN (Fig. 2d) from Supplementary Fig. 4 considering $\phi_{\mathrm{refl}}=\pi/4$ (ref. [28]). This analysis clearly shows that STEM–EELS can supply ultrahigh momentum compensation, so the resolved phonon polaritons cover nearly the whole RS band. For comparison, we also plot the momentum detection range of s-SNOM (purple dashed rectangle in Fig. 2d), which is less than one-tenth of that provided by EELS.

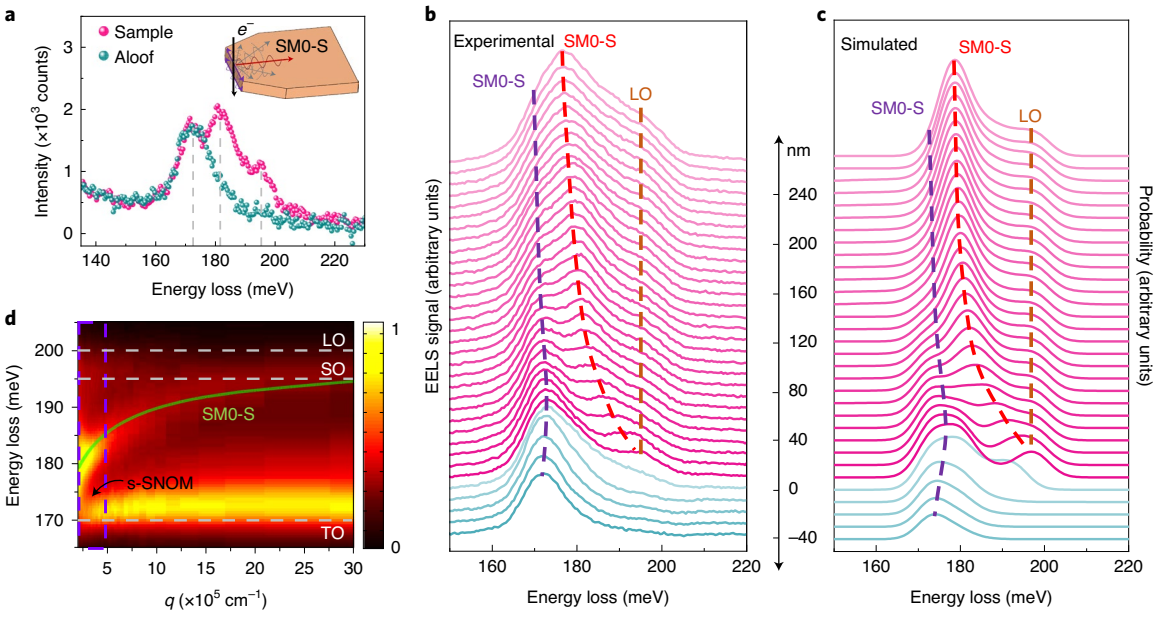

Fig. 2 | Electron energy-loss spectra of the h-BN flake with thickness of 10 nm. a, EELS spectra acquired at two positions inside (Sample, magenta dotted line) and outside (Aloof, cyan dotted line) the h-BN flake. The inset shows the schematic of a 10-nm-thick suspended h-BN nanoflake. The electron beam (black arrow) is incident perpendicularly on the h-BN plane and excites phonon polaritons propagating along the sample. **b**,**c**, Experimental (**b**) and simulated (**c**) EELS data of the h-BN flake acquired at different positions. The magenta and cyan colours are used to distinguish spectra acquired inside and outside the sample, respectively. The violet, red and brown dashed lines are guides for the eye for SM0-S (low q), SM0-S (high q) and LO modes, respectively. The difference between the left and central peaks is schematically shown in the inset of **a**. **d**, Calculated dispersion relation of h-BN from **b**, with the colour scale indicating the EELS intensity in arbitrary units. The green line is a FEM simulation. The typical wave vector detection range of scatting-type near-field optical method (s-SNOM) is denoted by a violet dashed rectangle. The three white dashed lines indicate the energy of TO, LO and SO phonons of h-BN.

By plotting the LO, SO and TO modes (horizontal dashed lines in Fig. 2d) together with the HPhP dispersion, we find that it asymptotically approaches the SO phonon as the wave vector increases. This implies that this peak should be assigned to the surface phonon polariton due to the small size of the h-BN flake (the minimum width is 170 nm), where Fabry–Pérot cavity resonance takes place[19]. The FEM calculations indicate that this peak is consistent with the symmetric mode of the surface phonon polariton (SM0-S mode, pink solid curve in Fig. 2d, details Supplementary Notes).

The left peak can be observed in both bulk and aloof measurements. It is close to the TO phonon, but is not the TO phonon because that cannot be electrically excited[29]. FEM calculations (Supplementary Fig. 5) allow us to ascribe it to the SM0-S mode, which is the same mode as the central peak[30,31]. The frequency difference between the left and central peaks is due to the different wave vectors[24]. The central peak originates in the constructive interference of the HPhPs reflected by the edge and the excited HPhPs, and its q depends on position ($2q|d| + \phi_{\mathrm{refl}} = 2\pi$). The left peak has a much lower and unchangeable q with position, since it arises due to the excitation of HPhPs propagating along the direction perpendicular to the electron-beam line scan. The small blue shift of the left peak as the beam approaches the edge suggests that it is the convolution of several peaks with different frequencies and that the peaks with higher frequencies have larger spatial extension (as shown in Supplementary Fig. 2a)[24]. Since the two peaks are essentially the same, their frequencies become equal in the position far away from the edge of h-BN (edge reflection is negligible). It should be pointed out that the aloof excitation of polaritons cannot be achieved by using external optical meathods[32–34]. Overall, the spatial distribution of the three features observed through 2D EELS mapping further supports their assignment as LO, SM0-S (low q) and SM0-S (high q) modes, respectively (Supplementary Fig. 6 and related discussion in Supplementary Information).

Ultra-confined HPhPs in suspended h-BN monolayer

Following this approach, we measure the HPhPs of monolayer h-BN. The waveguide modes of semi-infinite monolayer h-BN are schematically presented in the upper-left inset in Fig. 3a. An atomically resolved image of the suspended monolayer h-BN displays the typical different brightness of the B and N atoms (see upper-right inset in Fig. 3a). Figure 3a shows a series of EELS spectra as the electron beam moves from aloof to inside the monolayer h-BN. In contrast to multilayer h-BN (Fig. 2b), there is only one resonance peak observed in the monolayer sample (the vibrational signal of amorphous carbon is removed as explained in Supplementary Fig. 7; see Supplementary Fig. 7c for the original data). This peak can exist in both aloof and in-sample geometries, thus demonstrating that HPhPs exist in monolayer h-BN.

We also perform FEM simulations to further understand EELS in suspended monolayer h-BN (see details in Supplementary Notes). Here, the monolayer h-BN is considered as a semi-infinite film, rather than the actual microstructure, owing to the large suspended area (>2 × 2 μm²). The calculation uses the 2D conductivity $\sigma(\omega)$ of monolayer h-BN, fitted to theory as follows[12]:

$$\sigma(\omega) = \frac{-4i\epsilon_0\epsilon_{\mathrm{env}}\omega\omega_{\mathrm{TO}}v_{\mathrm{g}}}{\omega_{\mathrm{TO}}^2 - \omega^2 - i\omega\tau^{-1}} \quad (1)$$

where $\epsilon_{\mathrm{env}} = 1$, $\omega_{\mathrm{TO}} = 1{,}387\,\mathrm{cm}^{-1}$, $\tau^{-1} = 5\,\mathrm{cm}^{-1}$, $v_{\mathrm{g}} = 1.2 \times 10^{-4}c$ and ϵ_0 is the permittivity of free space. The dielectric function becomes $\epsilon_{\mathrm{Q2D}}(\omega) = (\hat{\mathbf{x}} \otimes \hat{\mathbf{x}} + \hat{\mathbf{y}} \otimes \hat{\mathbf{y}})\epsilon_{\mathrm{Q2D},||} + \hat{\mathbf{z}} \otimes \hat{\mathbf{z}}\epsilon_{\mathrm{Q2D},\perp}$ (ref. [12]), where $\epsilon_{\mathrm{Q2D},\perp} = 1$ and

$$\epsilon_{\mathrm{Q2D},||}(\omega) = 1 + \frac{i\sigma}{\epsilon_0\omega t} = 1 + \frac{1}{t}\frac{4\epsilon_{\mathrm{env}}\omega_{\mathrm{TO}}v_{\mathrm{g}}}{\omega_{\mathrm{TO}}^2 - \omega^2 - i\omega\tau^{-1}} \quad (2)$$

assuming a monolayer thickness $t = 0.34$ nm. Supplementary Fig. 8 shows the imaginary part of the dielectric function of monolayer

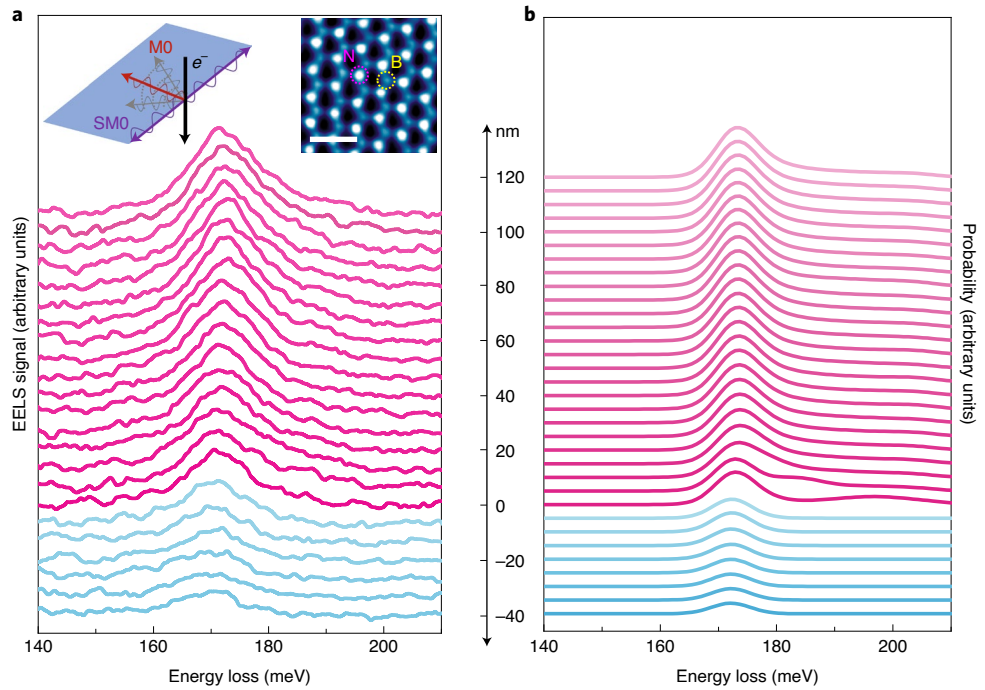

Fig. 3 | EELS spectra of monolayer h-BN. a, EELS spectra acquired along a line normal to the sample edge. The upper-left inset shows the schematic of waveguide modes in a semi-infinite monolayer h-BN. The black arrow represents the electron beam. Waveguide modes spread from the position of the electron beam with a semicircular wavefront. The M0 and SM0 modes are denoted by red and violet arrows. The upper-right inset shows an atomic HAADF image of the measured monolayer h-BN sample, in which bright N and dim B atoms are highlighted. Scale bar, 0.5 nm. **b**, Simulated EELS spectra of the monolayer h-BN flake corresponding to **a**. Magenta and cyan colours are used to distinguish spectra acquired inside and outside the sample, respectively.

h-BN as $\mathrm{Im}\{-1/\epsilon_{\mathrm{Q2D},||}\}$, which is proportional to the LO phonon signal. The detection of no corresponding LO peak directly indicates that LO and TO are degenerated into one point.

Using this dielectric function, we calculate the EELS spectra (Fig. 3b, details in Supplementary Fig. 9), which show good agreement with the experimental data (Fig. 3a). The peak observed in the aloof configuration corroborates that the HPhP modes can be detected in monolayer h-BN and the excitation efficiency decreases as the electron beam moves away from the edge. The simulation implies that the detected single peak is actually the combination of two peaks, that is, low-q and high-q HPhPs. There are two peaks in the calculated pristine EELS spectra without convolution with the ZLP (Supplementary Fig. 9a). However, they are too close to be resolved after introducing the ZLP tail and broadening. The low-q HPhP feature is similar to the left peak in Fig. 2b, which occurs in the aloof configuration and does not change with beam position. Thus, it can be assigned to the SM0 mode propagating along the boundary of the monolayer h-BN flake. The high-q HPhP feature is similar to the central peak in Fig. 2b, mainly due to constructive interference between incident and edge-reflected HPhPs, so it changes with d. As the incident electron beam is inside, far away from the h-BN edge, edge reflection becomes negligible, and, therefore, the frequency of HPhPs reaches a steady value (Fig. 3b and Supplementary Fig. 10).

Figure 4a compares the dispersion of HPhP modes in h-BN flakes with different thicknesses, ranging from monolayer to thin (~3, 4 and 10 nm) and thick (~116 nm) samples. For the ultrathin h-BN samples (~3, 4 and 7 nm, details in Supplementary Fig. 11), the experimental dispersion agrees well with that of the calculated SM0-S mode (solid curves), which further corroborates the mode assignment. The difference between the experimental and calculated dispersion in monolayer h-BN could be attributed to the fact that the former is not a pure fundamental mode, but a combination of the high- and low-q HPhPs, as discussed above. We extract the peak values of the simulated high-q HPhPs as red squares, which agree well with the theoretical dispersion. We want to stress that thinner h-BN samples exhibit much flatter HPhP dispersion curves, thus requiring higher momentum compensation to excite their HPhPs. As shown, the phonon polaritons over nearly the entire upper RS band on these thin h-BN samples can be detected by STEM–EELS (corresponding to momentum compensation of about $10^6\,\mathrm{cm}^{-1}$). Additionally, a field confinement (q/q_0) of 300 can be easily achieved in sub-10-nm h-BN, and even much higher confinement (>487) can also be observed in these thin samples (Supplementary Fig. 12). In contrast, it is challenging to detect the high-momentum HPhPs via optical characterization, as we confirm by performing s-SNOM measurements in a 116-nm h-BN sample, where HPhPs are observed only in a very limited momentum range (for details see Supplementary Fig. 13).

HPhPs in monolayer and even sub-10-nm h-BN display ultrahigh wavelength confinement, which largely breaks the optical diffraction limit and enhances the interaction between light and matter, further increased by the slow group velocity of these modes. In Fig. 4b, we calculate the group velocity $v_g = \partial\omega/\partial q$ of h-BN phonon polaritons from their dispersion relation observed in monolayer, 10-nm and 116-nm-thick samples. By resorting to electron-beam excitation, we can achieve ultrahigh confinement in monolayer h-BN. In addition, we can also resolve polariton group velocities as low as $10^{-5}c$, which is one to two orders of magnitude lower than previous observations of slow polaritons in h-BN by means of optical excitation techniques[26]. These ultraslow group velocities will further enhance the light–matter interaction while reducing the propagation length of phonon polaritons[35].

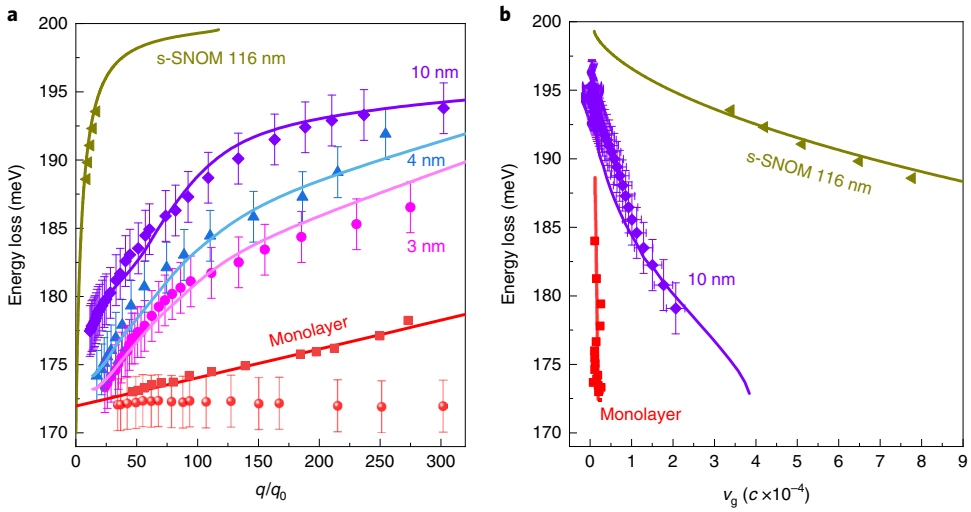

Fig. 4 | Ultraslow group velocity in monolayer h-BN. a, Dispersion of phonon polaritons in h-BN flakes with different thicknesses. The dots with error bars represent experimental data while the solid curves correspond to FEM simulations. The red squares of monolayer h-BN are extracted from M0 modes in the unconvoluted simulation spectra (see Supplementary Fig. 9a). The red circles with error bars are extracted from the HPhPs in Fig. 3a. The error bars are the extraction deviation of EELS experiment data. **b**, Calculated group velocities of the fundamental mode (that is, the M0 for the semi-infinite monolayer and the 116-nm-thick h-BN film; SM0-S for the 10-nm-thick h-BN with the antenna structure) as obtained from the polariton dispersion in **a** using the equation $v_g = \partial\omega/\partial q$. The error bars in the *y*-axis direction are the same as in **a**. The error bars in the *x*-axis direction are calculated from the *y*-axis direction using the error propagation rule.

Discussion and outlook

We want to stress that ultra-confined polaritons enable the design of ultra-compact optical devices, and lead to strong light–matter interaction and intriguing quantum phenomena[36–38]. To date, the highest observed confinement was realized by compressing graphene plasmons in a graphene/h-BN/Au heterostructure, which is limited to below 300 because the effective gap is actually 3 nm due to the nonlocal field penetration[38]. In contrast, free electrons bear an inherent advantage by supplying high momentum because of their finite mass. As one is interested in accessing polariton wave vectors as large as $2q|d| + \phi_{\mathrm{refl}} = 2\pi$, the detection of electronic excitations highly depends on the spatial resolution of EELS. STEM–EELS has highest spatial resolution, 0.2 nm in our case, which involves a momentum compensation up to $10^8\,\mathrm{cm}^{-1}$. On the basis of this powerful technique, we probe HPhPs covering nearly the entire upper RS band and the whole phonon dispersion in free-standing sub-10-nm-thick h-BN flakes (3, 4, 7 and 10 nm). More importantly, we have revealed polaritons in monolayer h-BN.

Phonon polaritons are expected to exist in the RS bands, but these bands disappear in monolayer h-BN, since the LO and TO phonons are degenerate at the Γ point. This raises the intriguing question of what the phonon polaritons should be like under this condition. By the direct observation of phonon polaritons in suspended monolayer h-BN, we prove that these HPhPs can exist in a spectral range above the TO frequency and exhibit ultrahigh confinement even at low wave vector. These highly confined HPhPs in monolayer h-BN are substantially different from the ultra-confined graphene plasmons in the graphene/h-BN/Au heterostructure[38]. When the plasmon velocity of the latter was down to about $c/250$ (that is, ~250 confinement), it approached the Fermi velocity of graphene, such that quantum nonlocal effects become appreciable and change the dispersion[37]. In contrast, the dispersion of HPhPs in dielectric h-BN can be well described by classical electromagnetic theory, which implies that quantum effects can be neglected since no Landau damping is at work.

By using the STEM–EELS technique with sub-10-meV energy resolution and sub-nanometre spatial resolution, we reveal HPhPs in monolayer h-BN with high confinement (>487) and ultraslow group velocity (down to about $10^{-5}c$). These results can find applications in ultrathin metasurfaces and enhanced light–matter interactions for sensing and spontaneous emission engineering. The observed high-momentum polaritons also open the field to the use of electron excitation as a source for investigating ultra-confined polaritons and their associated quantum phenomena, especially for the abundant but relatively unexplored polaritons in van der Waals materials.

Online content

Any methods, additional references, Nature Research reporting summaries, source data, extended data, supplementary information, acknowledgements, peer review information; details of author contributions and competing interests; and statements of data and code availability are available at https://doi.org/10.1038/s41563-020-0763-z.

Received: 2 January 2020; Accepted: 9 July 2020;
Published online: 17 August 2020

References

1. Basov, D. N., Fogler, M. M. & García de Abajo, F. J. Polaritons in van der Waals materials. *Science* **354**, aag1992 (2016).
2. Caldwell, J. D. et al. Photonics with hexagonal boron nitride. *Nat. Rev. Mater.* **4**, 552–567 (2019).
3. Low, T. et al. Polaritons in layered two-dimensional materials. *Nat. Mater.* **16**, 182–194 (2017).
4. Dai, S. et al. Subdiffractional focusing and guiding of polaritonic rays in a natural hyperbolic material. *Nat. Commun.* **6**, 6963 (2015).
5. Li, P. N. et al. Hyperbolic phonon-polaritons in boron nitride for near-field optical imaging and focusing. *Nat. Commun.* **6**, 7507 (2015).
6. Autore, M. et al. Boron nitride nanoresonators for phonon-enhanced molecular vibrational spectroscopy at the strong coupling limit. *Light Sci. Appl.* **7**, 17172 (2018).
7. Hu, H. et al. Gas identification with graphene plasmons. *Nat. Commun.* **10**, 1131 (2019).
8. Yang, X. et al. Nanomaterial-based plasmon-enhanced infrared spectroscopy. *Adv. Mater.* **30**, 1704896 (2018).
9. Guo, X. et al. High-efficiency modulation of coupling between different polaritons in an in-plane graphene/hexagonal boron nitride heterostructure. *Nanoscale* **11**, 2703–2709 (2019).

10. Li, P. et al. Infrared hyperbolic metasurface based on nanostructured van der Waals materials. *Science* **359**, 892–896 (2018).
11. Dai, S. et al. Tunable phonon polaritons in atomically thin van der Waals crystals of boron nitride. *Science* **343**, 1125–1129 (2014).
12. Rivera, N., Christensen, T. & Narang, P. Phonon polaritonics in two-dimensional materials. *Nano Lett.* **19**, 2653–2660 (2019).
13. Reich, S. et al. Resonant Raman scattering in cubic and hexagonal boron nitride. *Phys. Rev. B* **71**, 205201 (2005).
14. Rokuta, E. et al. Phonon dispersion of an epitaxial monolayer film of hexagonal boron nitride on Ni(111). *Phys. Rev. Lett.* **79**, 4609–4612 (1997).
15. Serrano, J. et al. Vibrational properties of hexagonal boron nitride: inelastic X-ray scattering and ab initio calculations. *Phys. Rev. Lett.* **98**, 095503 (2007).
16. Dias, E. J. C. & García de Abajo, F. J. Fundamental limits to the coupling between light and 2D polaritons by small scatterers. *ACS Nano* **13**, 5184–5197 (2019).
17. Dai, S. Y. et al. Phonon polaritons in monolayers of hexagonal boron nitride. *Adv. Mater.* **31**, e1806603 (2019).
18. Fei, Z. et al. Infrared nanoscopy of dirac plasmons at the graphene-SiO_2 interface. *Nano Lett.* **11**, 4701–4705 (2011).
19. Alfaro-Mozaz, F. J. et al. Nanoimaging of resonating hyperbolic polaritons in linear boron nitride antennas. *Nat. Commun.* **8**, 15624 (2017).
20. García de Abajo, F. J. Optical excitations in electron microscopy. *Rev. Mod. Phys.* **82**, 209–275 (2010).
21. Dwyer, C. et al. Electron-beam mapping of vibrational modes with nanometer spatial resolution. *Phys. Rev. Lett.* **117**, 256101 (2016).
22. Batson, P. E. & Lagos, M. J. Characterization of misfit dislocations in Si quantum well structures enabled by STEM based aberration correction. *Ultramicroscopy* **180**, 34–40 (2017).
23. Krivanek, O. L. et al. Vibrational spectroscopy in the electron microscope. *Nature* **514**, 209–212 (2014).
24. Govyadinov, A. A. et al. Probing low-energy hyperbolic polaritons in van der Waals crystals with an electron microscope. *Nat. Commun.* **8**, 95 (2017).
25. Hage, F. S. et al. Nanoscale momentum-resolved vibrational spectroscopy. *Sci. Adv.* **4**, eaar7495 (2018).
26. Li, P. et al. Optical nanoimaging of hyperbolic surface polaritons at the edges of van der Waals materials. *Nano Lett.* **17**, 228–235 (2017).
27. Konecna, A. et al. Vibrational electron energy loss spectroscopy in truncated dielectric slabs. *Phys. Rev. B* **98**, 205409 (2018).
28. Kang, J. H. et al. Goos–Hänchen shift and even–odd peak oscillations in edge-reflections of surface polaritons in atomically thin crystals. *Nano Lett.* **17**, 1768–1774 (2017).
29. Fuchs, R. Theory of the optical properties of ionic crystal cubes. *Phys. Rev. B* **11**, 1732–1740 (1975).
30. Caldwell, J. D. et al. Low-loss, infrared and terahertz nanophotonics using surface phonon polaritons. *Nanophotonics* **4**, 44–68 (2015).
31. Qi, R. et al. Probing far-infrared surface phonon polaritons in semiconductor nanostructures at nanoscale. *Nano Lett* **19**, 5070–5076 (2019).
32. Hu, F. et al. Imaging exciton-polariton transport in $MoSe_2$ waveguides. *Nat. Photon.* **11**, 356–360 (2017).
33. Fei, Z. et al. Gate-tuning of graphene plasmons revealed by infrared nano-imaging. *Nature* **487**, 82–85 (2012).
34. Chen, J. et al. Optical nano-imaging of gate-tunable graphene plasmons. *Nature* **487**, 77–81 (2012).
35. Cusco, R. et al. Isotopic effects on phonon anharmonicity in layered van der Waals crystals: isotopically pure hexagonal boron nitride. *Phys. Rev. B* **97**, 155435 (2018).
36. Basov, D. N. & Fogler, M. M. Plasmonic imaging is gaining momentum. *Science* **357**, 132–133 (2017).
37. Lundeberg, M. B. et al. Tuning quantum nonlocal effects in graphene plasmonics. *Science* **357**, 187–190 (2017).
38. Alcaraz Iranzo, D. et al. Probing the ultimate plasmon confinement limits with a van der Waals heterostructure. *Science* **360**, 291–295 (2018).

Methods

Sample preparation and treatment for TEM experiments. Hexagonal boron nitride flakes were prepared by exfoliating BN particles in *N*-methyl-2-pyrrolidone (NMP), following a published procedure[39,40]. The BN powders (~500 mg) were exfoliated by NMP (1,000 ml) in a low-power sonic bath for 1 h. The supernatant after centrifugation was dispersed in 50 ml of ultrapure water and then filtered against a polytetrafluoroethylene membrane (0.45 μm) ten times[41]. The final filter cake was dispersed in pure ethanol in an ultrasonic oscillator for 10 min, and then three droplets of the solution were transferred onto the 3-mm lacy carbon TEM grid. The monolayer samples were prepared by atmospheric pressure chemical vapour deposition with BH_3NH_3 powder as the precursor. The commercial Cu foils (25 μm thick, Alfa Aesar) were first treated with diluted nitric acid, and then annealed at 1,000 °C in the forming gas for 10 min. The growth was initialized by heating the precursor at 120 °C and the growth duration was typically 10–30 min, followed by fast cooling. Before the TEM experiments, the samples were annealed at 160 °C for 8 h to remove any hydroxide contamination.

EELS and imaging experiments. EELS experiments were carried out at a monochromatic Nion U-HERMES200 electron microscope operated at 60 kV with a convergence semi-angle $\alpha = 15$ mrad and a collection semi-angle $\beta = 24.9$ mrad. Since the momentum transfer required to excite polaritons is very small (~1/200 of the first Brillouin zone of h-BN), they can always be excited during practical operations regardless of the magnitude of the convergence angle. During experiment, once we centred the (000) diffraction spot in the EELS aperture, a larger collection angle than the convergence angle ensured that all the polariton signals were collected. The typical beam current was ~12 pA. The spectral sampling was chosen as 0.466 meV per channel (2,048 channels in total) to reduce the ZLP tail[42]. The EELS data of Fig. 2a were acquired over a 300-nm-long rectangle of 100 × 100 pixels, namely, using spatial steps of 3 nm per pixel in the map. Considering the balance between the scanning region and signal-to-noise ratio for each pixel during mapping, we found that 3 nm per pixel was a good choice to extract the polariton features of h-BN, although in principle we can achieve a spatial resolution down to 0.1 nm at 60 kV by adjusting the convergence angle and scanning region. Each spectrum in Fig. 2a was accumulated during 40 acquisitions at points parallel to the edge. The ZLP is slightly saturated (dwell time 100 ms per pixel) to optimize the signal-to-noise ratio of the phonon. For the momentum-resolved EELS experiments, a convergence semi-angle $\alpha = 1.5$ mrad was used, while the collection angle was specified by the slot aperture to $\beta_1 \times \beta_2 \sim 3 \times 50$ mrad, which is different from the set-up reported recently[43]. The beam current was also ~11 pA. HAADF images in Fig. 1b and the inset of Fig. 3a were both acquired at the conditions of $\alpha = 35$ mrad and $\beta = (80, 210)$ mrad operated at 60 kV. These images were further denoised by the block-matching and 3D filtering (BM3D) method[44].

EELS data processing. *Preprocessing.* Raw data were first aligned by ZLP correction method using the Gatan Digital Micrograph Suite (GMS, v.2.32.888.0). Then, we normalized the spectra using the left part of the ZLP[45] (its integral in the range from −200 meV to −5 meV) and found that this method worked well for saturated spectra. We subsequently used a power-law method to remove the background, with two windows of ~0.13–0.15 eV and ~0.22–0.25 eV, to extract phonon signals over the range ~0.17–0.20 eV .

Gaussian peak fit. We used a multi-Gaussian peak-fitting method to extract the three polariton peaks from the composed signal. The experimental spectra were first deconvoluted with a Gaussian peak to eliminate the effects of the ZLP tail of the electron beam[42]. Then we used one peak to fit the signals in vacuum, and three peaks to fit the signals in the bulk region. Every single spectrum from the 100 × 100 pixel EELS mapping was processed individually using the above method (see Supplementary Fig. 6 for an example of the fitting results).

ω–q data processing. To determine the full dispersion curve of the h-BN phonon, we used 10 s acquisition time per frame and accumulated 180 frames. Thus, the total acquisition time was 30 min. Alignment between frames and signals on each map were performed on the dataset. The *ω–q* map was then processed by the second-derivative method, which is conventionally used for EELS signals[46,47].

Thickness determination. The thickness of the h-BN flake was calculated using the log-ratio method[48] (that is, from the intensity ratio of plasmon losses to the ZLP). To increase the accuracy of calculation, the ZLP was unsaturated and the spectrum included as much plasma signal as possible. Thus, we acquired EELS spectra from −5 to ~ 95 eV, and processed them in the GMS (v.2.32.888.0) with the built-in log-ratio function to calculate the thickness.

Theoretical calculations. *FEM simulations.* The lower RS band covers the frequency range of two A_{2u} phonon modes ($\omega_{TO} = 97$ meV, $\omega_{LO} = 103$ meV), which have type-I hyperbolicity ($\epsilon_{\parallel} < 0$, $\epsilon_{\perp} > 0$). The upper RS band lies in the spectral range between two E_{1u} phonon modes ($\omega_{TO} = 170$ meV, $\omega_{LO} = 200$ meV), which show type-II hyperbolicity ($\epsilon_{\perp} < 0$, $\epsilon_{\parallel} > 0$). The h-BN permittivity can be approximated by[9,49]

$$\epsilon_m = \epsilon_{m,\infty}\left[1 + \frac{\omega_{LO,m}^2 - \omega_{TO,m}^2}{\omega_{TO,m}^2 - \omega(\omega + i\gamma_m)}\right], \quad (3)$$

where the labels $m = \perp$ and $\parallel$ refer to out-of-plane and in-plane polarization directions, respectively, whereas the other parameters in this expression are $\epsilon_{\perp,\infty} = 4.87$, $\epsilon_{\parallel,\infty} = 2.95$, $\gamma_{\perp} = 0.6$ meV, $\gamma_{\parallel} = 0.5$ meV, $\omega_{LO,\perp} = 103$ meV, $\omega_{TO,\perp} = 97$ meV, $\omega_{LO,\parallel} = 200$ meV and $\omega_{TO,\parallel} = 170$ meV.

Following a well-established procedure[20], the electron beam is treated as a line current perpendicular to the sample surface[27,50,51],

$$\mathbf{j}(\mathbf{r}, t) = -e\hat{\mathbf{v}}\delta[\mathbf{r} - \mathbf{r}_e(t)], \quad (4)$$

describing a point charge $-e$ (the electron) moving with constant velocity v along a linear trajectory $\mathbf{r}_e(t) = \mathbf{R}_0 + vt\hat{\mathbf{z}}$, where $\mathbf{R}_0 = (x_0, y_0)$ defines the position of the electron beam on the sample plane. To analyse electron spectra, we performed the Fourier transform on this current, which reads $\mathbf{j}(\mathbf{r}, \omega) = -e\hat{\mathbf{z}}\delta[\mathbf{R} - \mathbf{R}_0]e^{i\omega z/v}$ in frequency space ω. The fast electron introduces an external evanescent field $\mathbf{E_0}(\mathbf{r},t)$ as it moves in vacuum. When it strikes on the h-BN sample, an induced field $\mathbf{E}^{ind}(\mathbf{r},t) = \mathbf{E}(\mathbf{r},t) - \mathbf{E_0}(\mathbf{r},t)$ is generated, where $\mathbf{E}(\mathbf{r},t)$ is the total field, as determined by the optical response of the h-BN film. This field acts back on the electron and produces a total energy loss

$$Q = e\int \mathbf{v} \cdot \mathbf{E}^{ind}[\mathbf{r}_e(t), t]\mathrm{d}t. \quad (5)$$

Expressing the field in equation (5) as a function of its time-Fourier transform, we can write the energy loss as $Q = \int \hbar\omega\Gamma_{EELS}(\omega)\mathrm{d}\omega$, where[20,24]

$$\Gamma_{EELS}(\omega) = \frac{ev}{2\pi\hbar\omega}\int \mathrm{Re}\left\{e^{-\frac{i\omega z}{v}}E_z^{ind}(z,\omega)\right\}\mathrm{d}z \quad (6)$$

is the probability per unit frequency that the electron experiences an energy loss $\hbar\omega$. EELS spectra simulated according to equation (6) for electrons passing near the linear edge of a 10-nm h-BN flake are presented in Supplementary Fig. 2a. For a quantitative comparison between theoretical results and experimental data, the former (Supplementary Fig. 2a) were convolved with a Gaussian of 7.5-meV FWHM (Supplementary Fig. 2b).

Boundary element method simulations. We used the MATLAB toolbox MBPBEM to solve Maxwell's equations based on the local continuum dielectric model[52]. About 3,400 boundary elements were used in the calculation.

Density functional theory ab initio calculations. Structural and electronic properties of bulk h-BN were performed using the Vienna ab initio Simulation Package (VASP)[53] within the projector augmented-wave[54] approach with LDA pseudopotentials[55] for dealing with the h-BN interlayer van der Waals interaction[15,56,57]. A Γ-centred mesh of **k**-point sampling within the tetrahedron scheme with Blöchl corrections and a plane-wave cut-off of 520 eV were used for the primitive unit cell. The phonon dispersions and vibrational modes were evaluated within the frozen-phonon method from the conjunction of VASP and the open source Phonopy[58] package, using a 5 × 5 × 2 supercell and a 6 × 6 × 6 **k**-mesh for force-constant calculations. A density functional perturbation theory[59] calculation was performed to obtain optical properties for the non-analytical correction and LO–TO splitting.

Data availability

The data presented in Figs. 1–4 are provided with the paper as source data. Any other relevant data are also available from the corresponding author upon reasonable request.

References

39. Coleman, J. N. et al. Two-dimensional nanosheets produced by liquid exfoliation of layered materials. *Science* **331**, 568–571 (2011).
40. Zhang, X. Y. et al. Dispersion of graphene in ethanol using a simple solvent exchange method. *Chem. Commun.* **46**, 7539–7541 (2010).
41. Zhao, C. et al. Carbon-doped boron nitride nanosheets with ferromagnetism above room temperature. *Adv. Funct. Mater.* **24**, 5985–5992 (2014).
42. Lagos, M. J., Truegler, A., Hohenester, U. & Batson, P. E. Mapping vibrational surface and bulk modes in a single nanocube. *Nature* **543**, 529–532 (2017).
43. Senga, R. et al. Position and momentum mapping of vibrations in graphene nanostructures. *Nature* **573**, 247–250 (2019).
44. Dabov, K., Foi, A., Katkovnik, V. & Egiazarian, K. Image denoising by sparse 3-D transform-domain collaborative filtering. *IEEE Trans. Image Process.* **16**, 2080–2095 (2007).
45. Hachtel, J. A., Lupini, A. R. & Idrobo, J. C. Exploring the capabilities of monochromated electron energy loss spectroscopy in the infrared regime. *Sci. Rep.* **8**, 5637 (2018).

46. Jia, X. et al. Anomalous acoustic plasmon mode from topologically protected states. *Phys. Rev. Lett.* **119**, 136805 (2017).
47. Zhang, S. Y. et al. Lattice dynamics of ultrathin FeSe films on $SrTiO_3$. *Phys. Rev. B* **97**, 035408 (2018).
48. Malis, T., Cheng, S. & Egerton, R. EELS log-ratio technique for specimen-thickness measurement in the TEM. *J. Electron Microsc. Tech.* **8**, 193–200 (1988).
49. Kumar, A., Low, T., Fung, K. H., Avouris, P. & Fang, N. X. Tunable light-matter interaction and the role of hyperbolicity in graphene-hBN system. *Nano Lett.* **15**, 3172–3180 (2015).
50. Raza, S. et al. Extremely confined gap surface-plasmon modes excited by electrons. *Nat. Commun.* **5**, 4125 (2014).
51. Wiener, A. et al. Electron-energy loss study of nonlocal effects in connected plasmonic nanoprisms. *ACS Nano* **7**, 6287–6296 (2013).
52. Hohenester, U. & Truegler, A. MNPBEM—a Matlab toolbox for the simulation of plasmonic nanoparticles. *Comput. Phys. Commun.* **183**, 370–381 (2012).
53. Kresse, G. & Furthmuller, J. Efficient iterative schemes for ab initio total-energy calculations using a plane-wave basis set. *Phys. Rev. B* **54**, 11169–11186 (1996).
54. Blochl, P. E. Projector augmented-wave method. *Phys. Rev. B* **50**, 17953–17979 (1994).
55. Kresse, G. & Joubert, D. From ultrasoft pseudopotentials to the projector augmented-wave method. *Phys. Rev. B* **59**, 1758–1775 (1999).
56. Kern, G., Kresse, G. & Hafner, J. Ab initio calculation of the lattice dynamics and phase diagram of boron nitride. *Phys. Rev. B* **59**, 8551–8559 (1999).
57. Cusco, R., Gil, B., Cassabois, G. & Artus, L. Temperature dependence of Raman-active phonons and anharmonic interactions in layered hexagonal BN. *Phys. Rev. B* **94**, 155435 (2016).
58. Togo, A. & Tanaka, I. First principles phonon calculations in materials science. *Scr. Mater.* **108**, 1–5 (2015).
59. Gajdos, M., Hummer, K., Kresse, G., Furthmuller, J. & Bechstedt, F. Linear optical properties in the projector-augmented wave methodology. *Phys. Rev. B* **73**, 045112 (2006).

Acknowledgements

This work was supported by the National Key R&D Programme of China (grant numbers 2016YFA0300903, 2016YFA0201600 and 2019YFA0307801), the National Natural Science Foundation of China (grant numbers 11888101, 11974023, 51672007, 51925203, 11674073, 51972074, 11974001 and U1932153), Key-Area Research and Development Programme of Guangdong Province (grant numbers 2018B030327001, 2018B010109009 and 2019B010931001), Bureau of Industry and Information Technology of Shenzhen (grant number 201901161512), the National Equipment Programme of China (grant number ZDYZ2015-1), the '2011 Programme' from the Peking-Tsinghua-IOP Collaborative Innovation Centre of Quantum Matter, the key programme of the Bureau of Frontier Sciences and Education, Chinese Academy of Sciences (grant number QYZDB-SSW-SLH021), the Key Research Programme of the Chinese Academy of Sciences (grant number ZDBS-SSW-JSC002), Youth Innovation Promotion Association CAS and CAS Interdisciplinary Innovation Team (grant number JCTD-2018-03), the European Research Council (advanced grant number 789104-eNANO), the Spanish MINECO (grant numbers MAT2017-88492-R and SEV2015-0522) and Beijing Natural Science Foundation (grant numbers 2192022 and Z190011). We thank the Electron Microscopy Laboratory at Peking University for the use of electron microscopes, C. L. Shi and T. C. Lovejoy from Nion for advice on EELS experiments and J. Feng from the International Centre for Quantum Materials, Peking University, for advice on DFT calculations.

Author contributions

The concept for the experiment was initially developed by P.G., Q.D. and X.Y. Hexagonal BN thin flakes were grown by Z.X. and monolayer h-BN by Yifei Li under the supervision of K.L. and L.L. STEM–EELS experiments were performed by N.L., assisted by R.S. and Yuehui Li under the direction of P.G. FEM simulations and s-SNOM experiments were performed by X.G. under the supervision of Q.D. and X.Y. DFT calculations of h-BN phonon dispersion curves were performed by T.Q. and MNPBEM simulations were performed by R.Q. under the supervision of P.G. Data processing and analysis were performed by N.L. and X.G. F.J.G.A. provided theoretical advice. N.L., X.G. and X.Y. wrote the manuscript with input from P.G. and Q.D. N.L. and X.G. contributed equally to this work. All authors discussed the results at all stages and participated in the development of the manuscript.

Competing interests

The authors declare no competing interests.

Additional information

Supplementary information is available for this paper at https://doi.org/10.1038/s41563-020-0763-z.

Correspondence and requests for materials should be addressed to X.Y., Q.D. or P.G.

Reprints and permissions information is available at www.nature.com/reprints.

nature research

https://doi.org/10.1038/s41563-020-0763-z

Supplementary information

Direct observation of highly confined phonon polaritons in suspended monolayer hexagonal boron nitride

In the format provided by the authors and unedited

Supplementary Information for

"Direct observation of highly confined phonon polaritons in suspended monolayer hexagonal boron nitride"

Ning Li[1,2,3,4,13], Xiangdong Guo[1,4,5,6,13], Xiaoxia Yang[1,5]*, Ruishi Qi[2], Tianyu Qiao[2], Yifei Li[7], Ruochen Shi[2,3], Yuehui Li[2,3], Kaihui Liu[6,8], Zhi Xu[9], Lei Liu[7], F. Javier García de Abajo[10,11], Qing Dai[1,5]*, En-Ge Wang[2,8,9,12], and Peng Gao[2,3,4,8]*

[1]Division of Nanophotonics, CAS Key Laboratory of Standardization and Measurement for Nanotechnology, CAS Center for Excellence in Nanoscience, National Center for Nanoscience and Technology, Beijing 100190, China.

[2]International Center for Quantum Materials, Peking University, Beijing 100871, China.

[3]Electron Microscopy Laboratory, School of Physics, Peking University, Beijing 100871, China.

[4]Academy for Advanced Interdisciplinary Studies, Peking University, Beijing 100871, China.

[5]Center of Materials Science and Optoelectronics Engineering, University of Chinese Academy of Sciences, Beijing 100049, China.

[6]State Key Laboratory for Mesoscopic Physics, School of Physics, Peking University, Beijing 100871, China.

[7]Department of Materials Science and Engineering, College of Engineering, Peking University, Beijing 100871, China.

[8]Collaborative Innovation Center of Quantum Matter, Beijing 100871, China.

[9]Songshan Lake Materials Lab, Institute of Physics, Chinese Academy of Sciences, Dongguan 523000, China.

[10]ICFO-Institut de Ciencies Fotoniques, The Barcelona Institute of Science and Technology, 08860 Castelldefels (Barcelona), Spain.

[11]ICREA-Institució Catalana de Recerca i Estudis Avançats, Passeig Lluís Companys 23, 08010 Barcelona, Spain.

[12] School of Physics, Liaoning University, Shenyang 110036, China.

[13] These authors contributed equally: Ning Li, Xiangdong Guo.

**emails:* yangxx@nanoctr.cn, daiq@nanoctr.cn, p-gao@pku.edu.cn.

Supplementary Notes:

1. Finite element method (FEM) simulations

EELS spectra are simulated by solving the Maxwell equations using a FEM based on the optical properties of h-BN (see Methods). The bulk h-BN permittivity is approximated as[1,2]

$$\epsilon_m = \epsilon_{m,\infty}\left[1 + \frac{\omega_{\mathrm{LO},m}^2 - \omega_{\mathrm{TO},m}^2}{\omega_{\mathrm{TO},m}^2 - \omega(\omega + i\gamma_m)}\right], \quad (1)$$

where the label $m = \perp$ and $\parallel$ refers to out-of-plane and in-plane polarization directions, respectively, whereas the other parameters in this expression are $\epsilon_{\perp,\infty} = 4.87$, $\epsilon_{\parallel,\infty} = 2.95$, $\gamma_\perp = 0.6$ meV, $\gamma_\parallel = 0.5$ meV, $\omega_{\mathrm{LO},\perp} = 103$ meV, $\omega_{\mathrm{TO},\perp} = 97$ meV, $\omega_{\mathrm{LO},\parallel} = 200$ meV and $\omega_{\mathrm{TO},\parallel} = 170$ meV. In the EELS experiments, electrons with a fixed kinetic energy of ~60 keV are directed along a linear path perpendicular to the surface of the h-BN sample. These fast electrons excite h-BN phonons and phonon polaritons, thereby transferring part of their kinetic energy to the h-BN sample. The resulting loss of kinetic energy is measured by an EELS detector that disperses electrons according to their energy. The total number of electrons recorded by the detector is normalized in order to obtain an energy loss spectrum (i.e., the EELS probability).

Following a well-established procedure[3], we calculate EELS probabilities based on the stopping experienced by the electron as a result of the self-induced electric field in the presence of the sample. We treat the electron as a classical point source of charge -*e*, which generates an external current density given by[4,5]

$$\mathbf{j}(\mathbf{r}, t) = -e\,\hat{\mathbf{v}}\,\delta[\mathbf{r} - \mathbf{r}_\mathrm{e}(t)], \quad (2)$$

where the electron is taken to move with constant velocity vector **v** oriented along *z*, following a linear trajectory $\mathbf{r}_\mathrm{e}(t) = \mathbf{R_0} + vt\,\hat{\mathbf{z}}$, where $\mathbf{R_0} = (x_0, y_0)$ defines the impact parameter on the plane of the sample. We now perform a temporal Fourier transform, so the current density can be recast in frequency space ω as a line current $\mathbf{j}(\mathbf{r}, \omega) = -e\,\hat{\mathbf{z}}\,\delta[\mathbf{R} - \mathbf{R_0}]e^{i\omega z/v}$, which is part of the input in the FEM method. This current gives rise to an external electric field $\mathbf{E_0}(\mathbf{r},t)$ during the electron motion, that is, an evanescent field accompanying the electron even in the absence of a h-BN sample. We denote $\mathbf{E}(\mathbf{r},t)$ the amplitude of the total electric field generated when the electron impinges on the h-BN sample, while the induced field is given by the difference $\mathbf{E}^{\mathrm{ind}}(\mathbf{r},t) = \mathbf{E}(\mathbf{r},t) - \mathbf{E_0}(\mathbf{r},t)$. The total

electron energy loss is due to the work exerted by the induced electric field acting back on the electron, that is,

$$\mathrm{Q} = e \int \mathbf{v} \cdot \mathbf{E}^{\mathrm{ind}}[\mathbf{r}_{\mathrm{e}}(t), t] dt. \quad (3)$$

At this point, it is convenient to time-Fourier transform the induced field (i.e., we resort to the FEM solution in frequency space as obtained from the above line source), so that the total energy loss can be decomposed into the contribution of different energy loss components $\hbar\omega$ as $\mathrm{Q} = \int \hbar\omega \, \Gamma_{EELS}(\omega) \, d\omega$, where[3,6,7]

$$\Gamma_{\mathrm{EELS}}(\omega) = \frac{ev}{2\pi\hbar\omega} \int \mathrm{Re}\left\{ e^{-\frac{i\omega z}{v}} E_z^{\mathrm{ind}}(z, \omega) \right\} dz. \quad (4)$$

is the EELS probability. In this expression we assume that each frequency component is indeed given the corresponding energy loss at that frequency. We note that the classical description using a local dielectric function of h-BN is valid only for small scattering angles[6]. Incidentally, we perform numerical electromagnetic simulations to accurately describe the processes involved in EELS in samples of nontrivial geometry, such as film edges; we corroborate the validity of these calculations by finding good agreement with analytical theory for extended fields.

We calculate the EELS probability for a 10 nm h-BN flake according to Eq. (4). The result is shown in Supplementary Fig. 2a. We consider the flake to be a hexagonal prism as shown in Fig. 1a and the inset of Fig. 2a. For a quantitative comparison between experiment and theory, the spectral resolution determined by the measured ZLP needs to be considered, so we convolute the calculated spectrum of Supplementary Fig. 2a with a Gaussian distribution of 7.5 meV full width at half maximum (FWHM) (Supplementary Fig.2b):

$$\Gamma_{\mathrm{EELS}}^{\mathrm{broadened}}(\omega) = \int \mathrm{d}\omega' \, \Gamma_{\mathrm{EELS}}(\omega - \omega') \, \mathrm{ZLP}(\omega'). \quad (5)$$

Finally, we compute the EELS probability for different locations of the electron beam, as shown in Fig. 2c, which is in excellent agreement with experiment.

2. Boundary element method (BEM) simulations

We perform BEM simulations of EELS using the well-established MNPBEM Toolbox, which relies on the Green function of the Helmholtz equation to express the solution of the involved electromagnetic field as an integral extended over the boundaries of the sample materials, where auxiliary boundary charges and currents are self-consistently determined from the boundary conditions; this approach represents a substantial reduction in computation time compared with volume-based methods such as FEM. In practice, the surface of the h-BN flake is divided into thousands of boundary elements, but this method is difficult to apply to optically anisotropic materials such as h-BN, since it requires substantial modifications to introduce the anisotropic dielectric function into the model.

Both FEM and BEM simulations are based on a classical electrodynamics approach to describe the electron-sample interaction. They use numerical discretization to perform simulations of the electron energy-loss probability. Neglecting tiny change of the electron velocity during inelastic interaction with the sample --an approximation that is well justified for fast electrons--, the electron trajectory is modeled as a line current. It is assumed that the momentum transfer is small enough so that the permittivity of h-BN can be treated locally, that is, $\epsilon(\omega, q) \approx \epsilon(\omega, q = 0)$. When a fast electron beam passes through or near the material, it induces an electric field in it, which acts back on the electron. The resulting electron energy loss can thus be calculated by integrating the induced field along the beam trajectory, and spectrally separating it in different energy-loss components following a well-established procedure[3].

3. The Density Functional Theory (DFT)

An ab initio method is used here to calculate the structural and electronic properties of bulk h-BN. We perform these calculations within the Vienna ab initio Simulation Package (VASP)[8] using the projector augmented-wave approach[9] and the LDA functional[10] for dealing with the h-BN interlayer van der Waals interaction[11-13]. For further details of the calculation procedure, please see the Methods section in the main

text. Here, we summarize the model and the assumptions of this approach: firstly, we consider a conventional scattering model; an electron plane wave is considered to represent the fast electron beam with momentum $\mathbf{k}$ incident into the sample; the electron is then scattered to another momentum state $\mathbf{k}'$; as a result, the sample is exited from the initial ground state $|i\rangle$ into a final state $|f\rangle$; so the momentum $\mathbf{k}-\mathbf{k}'$ and energy $\omega=(k^2-k'^2)/2m$ transferred to the sample are translated into lateral deflection and energy loss of scattered electrons, respectively.

4. Analytical solution in the thin extended film limit

For an extended flake of negligible thickness compared with the surface polariton wavelength, the EELS probability under normal incidence far from the edge is given by[14]

$$\Gamma_{\mathrm{EELS}}(\omega)=\frac{4e^2}{\pi\hbar v^2}\int_0^\infty \frac{k_\parallel^2\,dk_\parallel}{\left(k_\parallel^2+\omega^2/v^2\right)^2}\,\mathrm{Im}\{r_\mathrm{p}\}, \tag{6}$$

where the integral extends over in-plane wave vector transfers $k_\parallel$, while $r_\mathrm{p}\approx k_\parallel/(k_\parallel-k_\mathrm{SP})$ is the Fresnel coefficient for p polarization, expressed in terms of the complex polariton wave vector $k_\mathrm{SP}=i\omega/2\pi\sigma$ (wavelength $2\pi/\mathrm{Re}\{k_\mathrm{SP}\}$, propagation distance $1/2\mathrm{Im}\{k_\mathrm{SP}\}$ for $1/e$ intensity decay), and this in turn as a function of the surface conductivity $\sigma(\omega)$. Using the Lorentzian expression shown for the latter in the main text, the integral in Eq. (6) admits the analytical solution

$$\Gamma_{\mathrm{EELS}}(\omega)\approx\frac{e^2}{\hbar v^2}\mathrm{Im}\left\{\left(\frac{1}{k_\mathrm{SP}}\right)\frac{3\vartheta+\vartheta^3+(2/\pi)[1+2\pi i+\vartheta^2+2\ln(\vartheta)]}{(1+\vartheta^2)^2}\right\} \tag{7}$$

with $\vartheta=\omega/(vk_\mathrm{SP})$. Supplementary Fig. 10 shows the result obtained from Eq. (7) for 60 keV electrons (red curve), revealing a spectral width slightly increased from the intrinsic damping rate γ as a result of integration over $k_\parallel$ in Eq. (6). This result corroborates the accuracy of our FEM simulations (black curve in Supplementary Fig. 10).

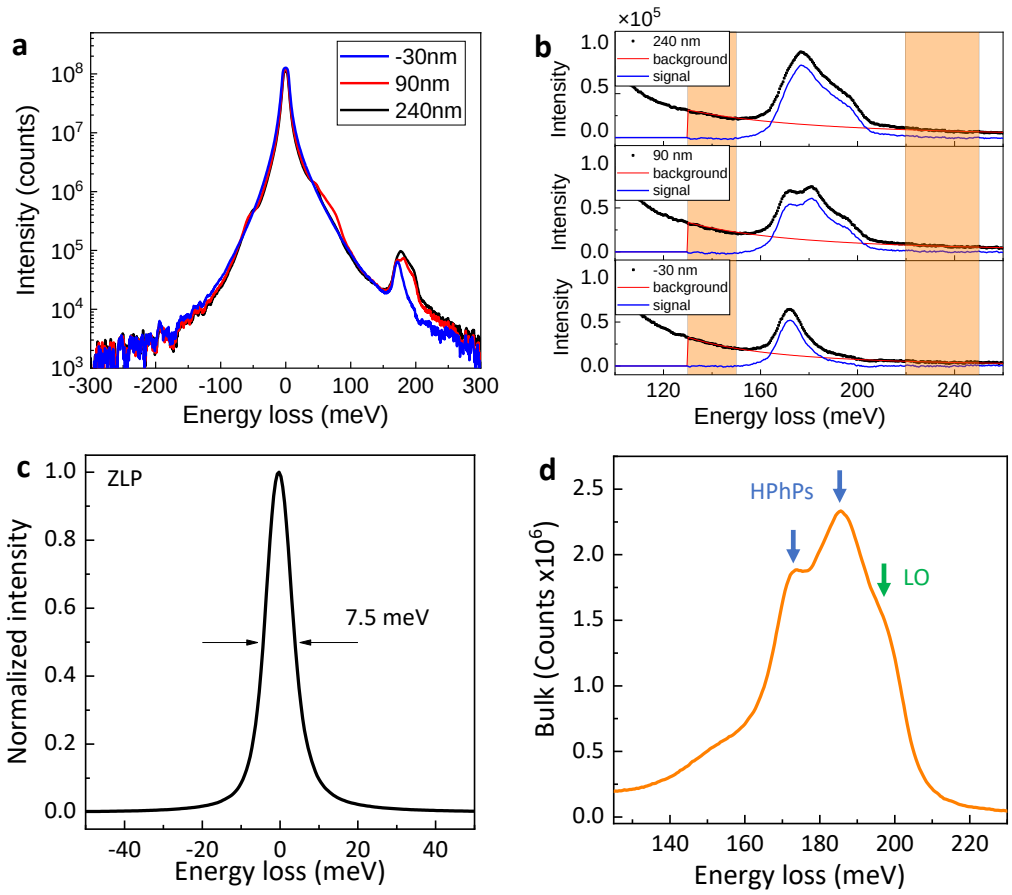

Supplementary Fig. 1 (a) Full spectra at positions -30 nm, 90 nm, and 240 nm in the sample of Fig. 2 in log scale. **(b)** Subtraction of vibrational signals with a power-law background model. To avoid being affected by the tail of the lower RS band, the two windows of 130-150 meV and 220-250 meV were used for all spectra. **(c)** Measured zero-loss peak (ZLP), which is found to have a FWHM of 7.5 meV, standing for the energy resolution of the microscope. **(d)** Spectrum acquired with an exposure time of 200 s, presenting several vibration modes.

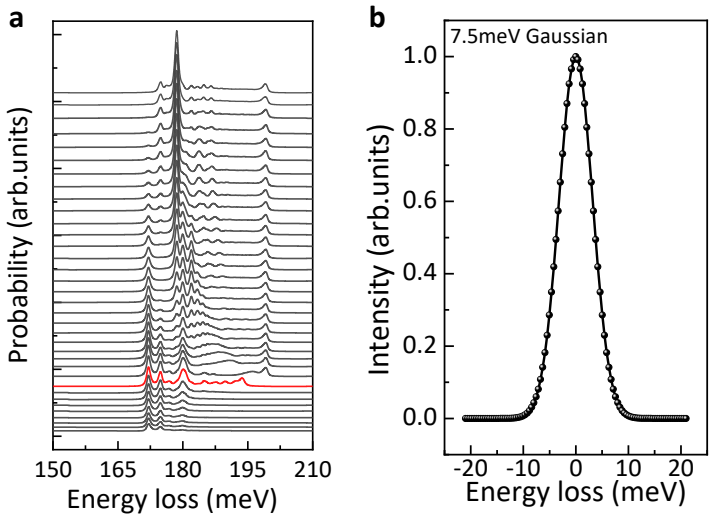

Supplementary Fig. 2. (a) Calculated EELS probability using FEM, before convolution with the ZLP. The red curve corresponds to the spectrum for the beam passing by the boundary of the h-BN flake. **(b)** Gaussian distribution of 7.5 meV FWHM used to convolute the calculation in (a) in order to compare theory and experiment in Fig. 2.

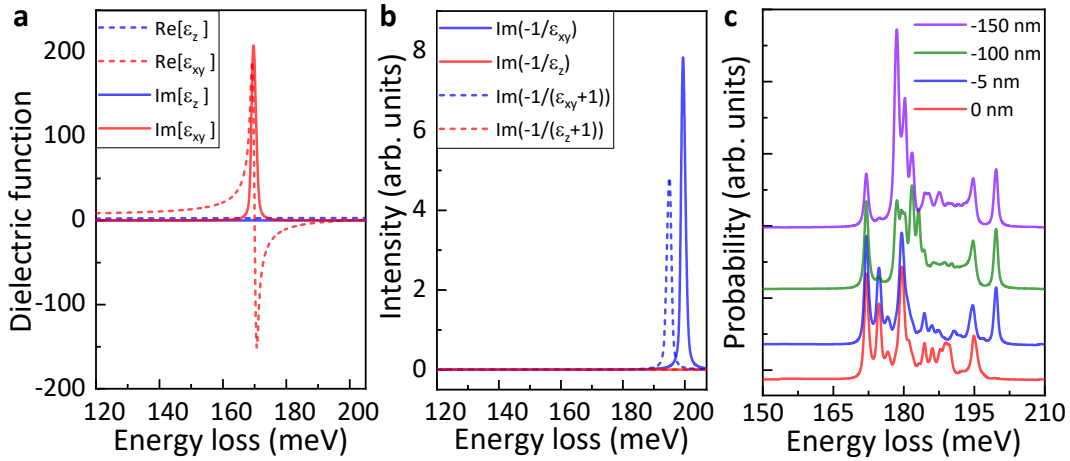

Supplementary Fig. 3. Dielectric properties of bulk h-BN. **(a)** Real and imaginary parts of the dielectric function (in-plane and out-of-plane polarization components $\varepsilon_{\parallel} \equiv \varepsilon_{xy}$ and $\varepsilon_{\perp} \equiv \varepsilon_{z}$, respectively). **(b)** Representative loss functions (see legend)[7]. These LO and SO phonons cannot be detected in optical experiments, which are limited by the transverse electromagnetic wave character of the light field. Optical methods detect the loss caused by a positive correlation with the imaginary part of the dielectric function of the material (i.e., $\propto \mathrm{Im}\{\varepsilon\}$). In contrast, electron-beam probing detects the electron energy-loss probability, which maps the imaginary part of the negative reciprocal of the dielectric function ($\propto \mathrm{Im}\{-1/\varepsilon\}$). **(c)** Calculated EELS probability for the isotropic case ($\varepsilon \equiv \varepsilon_{xy}$), which are different from the EELS probability for the anisotropic case in Supplementary Fig. 2a.

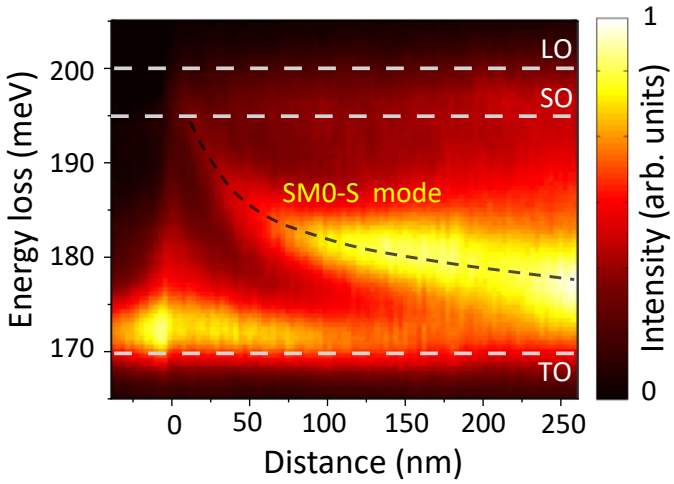

Supplementary Fig. 4. 2D view of the experimental dataset in Fig. 2b (after deconvolution) when the electron beam is located inside (positive distance), at the boundary (distance equal to 0) and outside (negative distance) of the 10 nm thick h-BN flake under investigation.

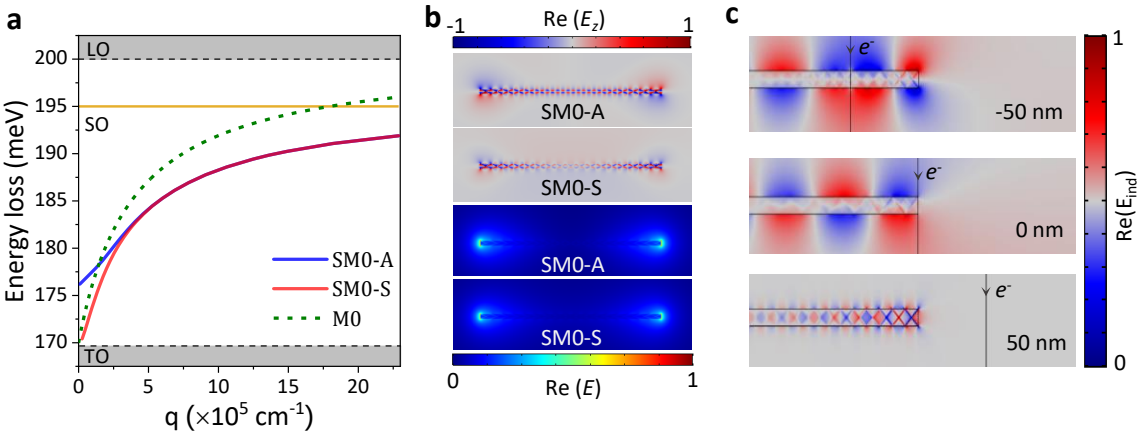

Supplementary Fig. 5. Dispersion of phonon polaritons and electromagnetic field distribution in 10 nm thick h-BN. **(a)** Dispersion curves of volume (M0, green-dashed curve), surface-symmetric (SM0-S, red-solid curve) and surface-asymmetric (SM0-A, blue-solid curve) modes. The FEM calculations display this central peak of Fig.2b is consistent with the symmetric mode of the surface phonon polariton (SM0-S mode in the 173-nm-width h-BN flake, pink solid curve in Fig. 2d, detail in Note 1, Supplementary Information). For comparison, we also calculate the dispersion of the bulk mode of the phonon polaritons (M0), which we find to be very different from the experimental data (refer to the dashed green line of Supplementary Fig. 5a). **(b)** Near-field distribution of SM0-A and SM0-S modes at 178 meV in the 10 nm thick h-BN (the flake maximum width is around 376 nm). **(c)** Cross section of the induced electric fields (*z*-component) taken at different positions of the electron beam in the 10-nm-thick semi-infinite h-BN.

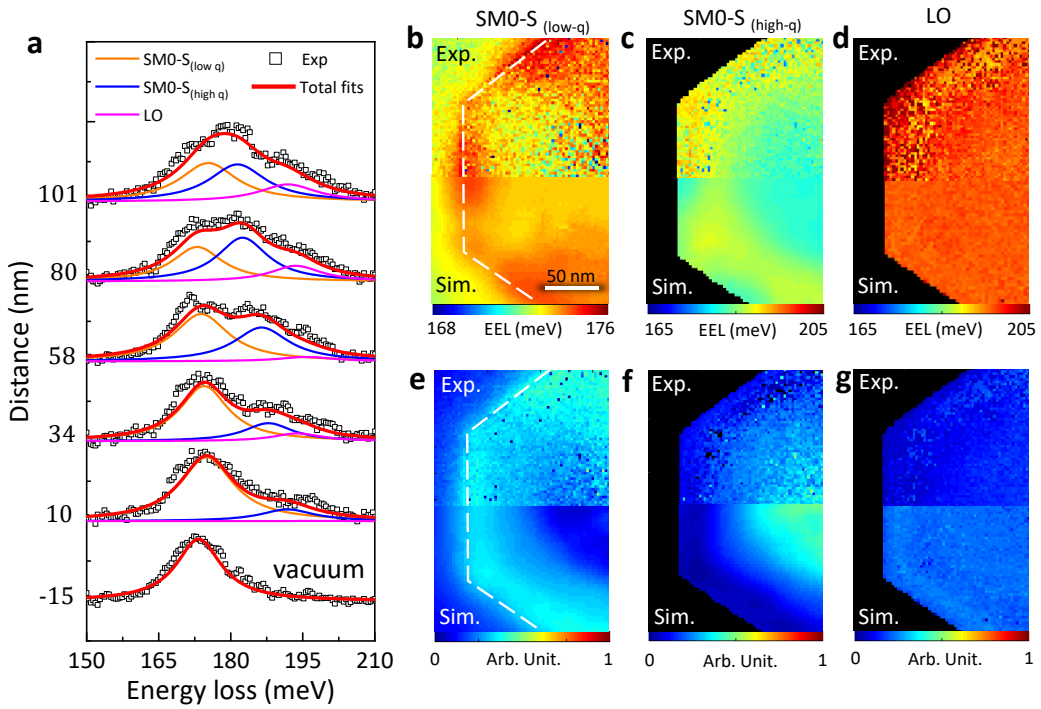

Supplementary Fig. 6. (a) Multi-Gaussian peak fitting method, showing how 3 vibrational signals are extracted from the raw measured data. **(b-d)** Spatial distribution of the energy of each mode. **(e-g)** Spatial distribution of the mode intensities. The calculated data (bottom parts of the plots in (b-g)) agree well with experimental data (upper parts). The SM0-$S_{(high-q)}$ mode only exists inside the h-BN flake and its frequency decreases gradually when entering inside the sample, as shown in (c). The intensity of this mode (f) is very low near the edge and becomes dominant inside the flake (~90 nm away from the edge). As shown in (b), at the edge the frequency of the SM0-$S_{(low-q)}$ mode reaches its largest value (175 meV). The SM0-$S_{(low-q)}$ mode is mainly localized at the edge of the h-BN flake with an attenuation distance of ~40 nm, which can be observed both inside and outside of the h-BN flake (e)[6]. Panels (d, g) demonstrate that the frequency and intensity of the LO mode are both uniform over the entire sample and mildly influenced by the edge[15].

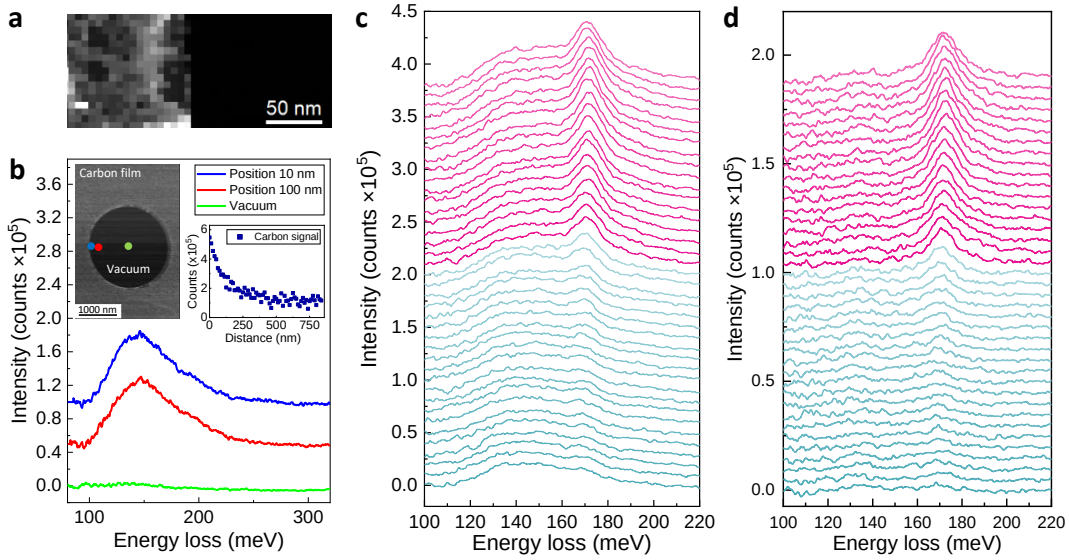

Supplementary Fig. 7. (a) Low magnification HAADF image of a monolayer h-BN sample corresponding the EELS mapping region**. (b)** EELS spectra acquired at 3 different positions near a bare amorphous carbon support film (see color-matching dots on the carbon support image in the upper-left inset), showing a wide vibration signal of amorphous carbon centered at ~150 meV. The upper-right inset shows a distance dependence of the ~150 meV signal intensity, revealing a decay length ~800 nm, which indicates that the influence of carbon support film cannot be neglected if the target signal is relatively weak. **(c)** EELS spectra of the line scan in (a); the influence of the carbon support film cannot be neglected here. **(d)** EELS spectra after subtraction of the amorphous carbon signal; each spectrum is calculated as $I_{\text{corrected}} = I_{\text{EELS}} - C \times I_{\text{carbon}}$, where the constant C is adjusted for each spectrum in order to have a position-insensitive intensity in the 120-180 meV range.

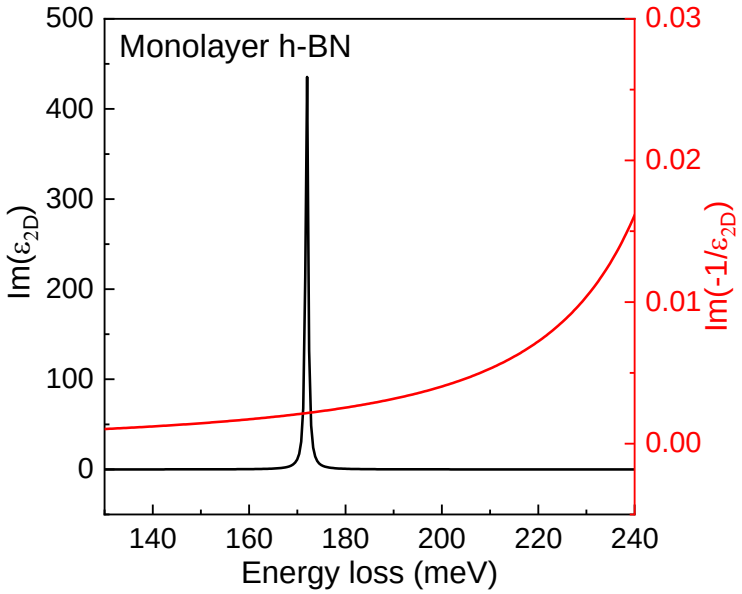

Supplementary Fig. 8. Imaginary parts of the dielectric function (black line, corresponding to TO) and representative loss function (red line, corresponding to LO) of monolayer h-BN.

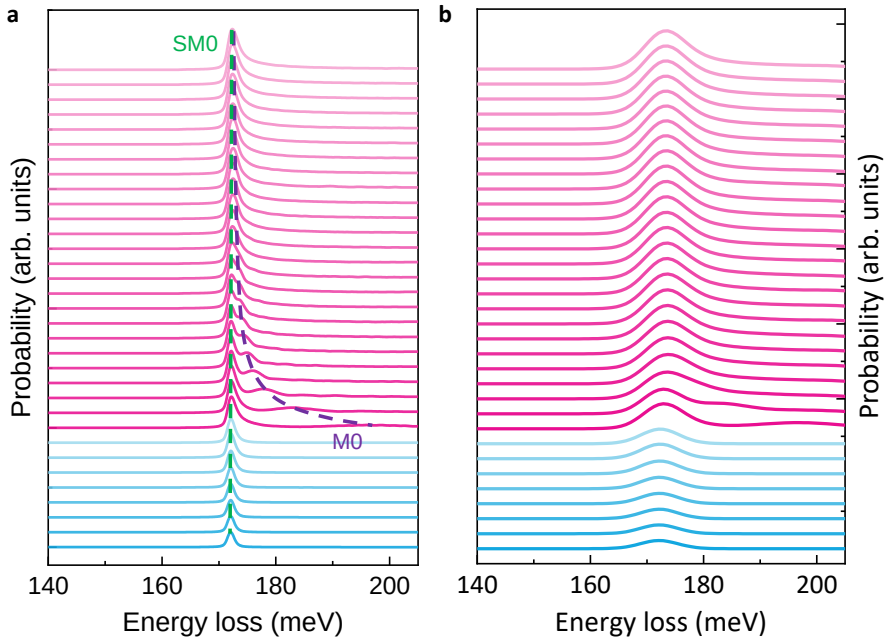

Supplementary Fig. 9. (a) Simulated EELS probability of monolayer h-BN using the FEM method. The green and purple dashed lines are guidelines of SM0 and M0 modes, respectively. **(b)** Same as (a) after convoluting with a 7.5 meV FWHM Gaussian peak.

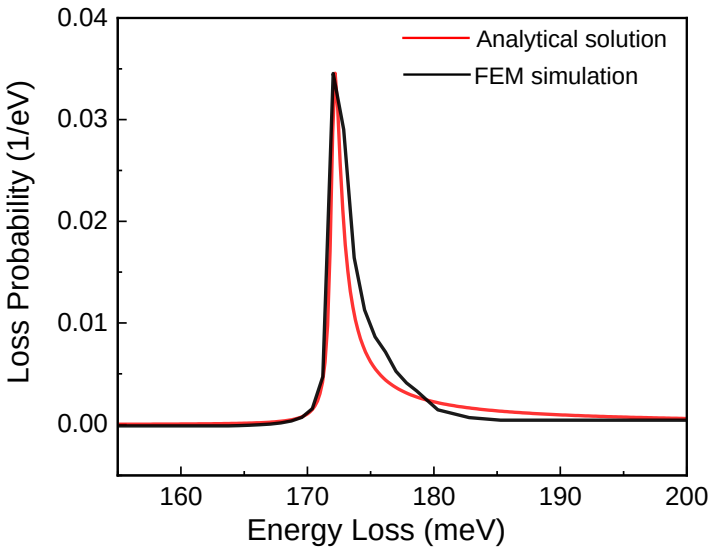

Supplementary Fig. 10. EELS probability simulation through FEM (black curve) and the rigorous analytical model of Eq. (6) (red curve) for 60 keV electrons crossing a monolayer h-BN film under normal incidence. The FEM curve is normalized to the maximum of the analytical one.

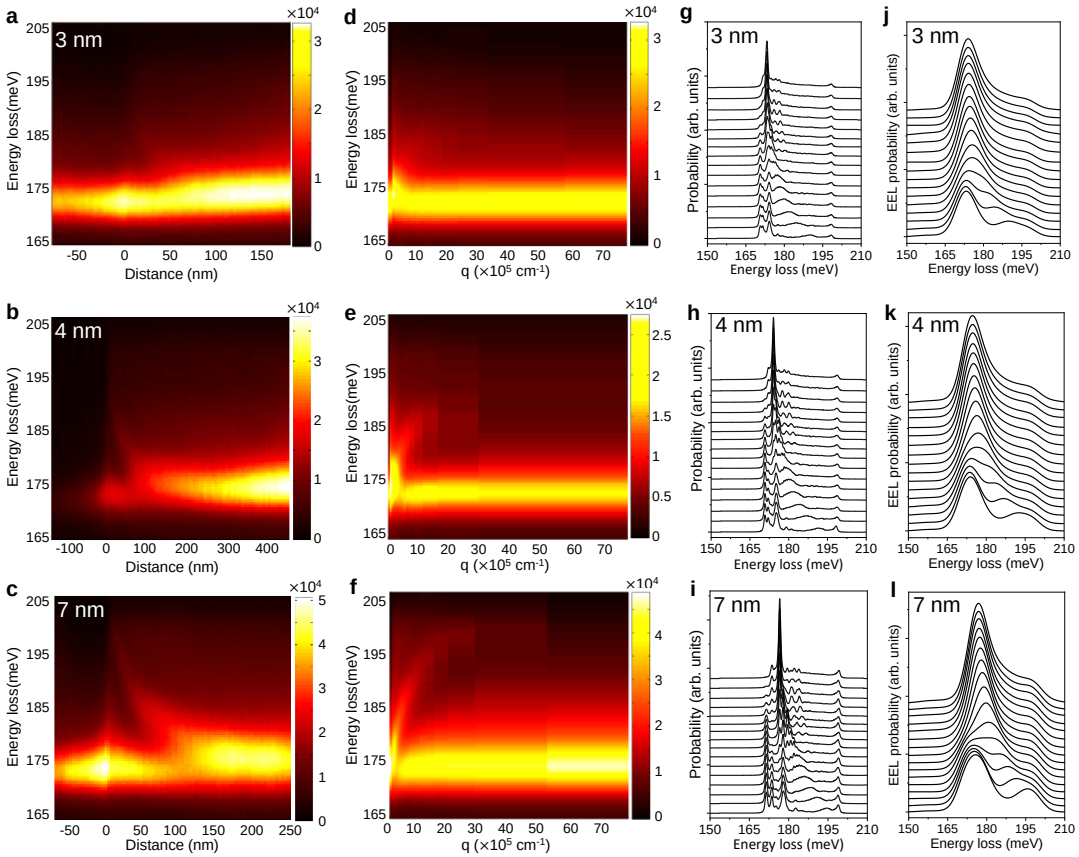

Supplementary Fig. 11. EELS measured data of h-BN flakes of ~3 nm, 4 nm and 7 nm thickness (upper, central and lower panel rows, respectively), along with our corresponding FEM calculations. **(a-c)** Position- and energy-loss-dependent EELS intensity. **(d-f)** Data from which we retrieve the dispersion of phonon polaritons from (a-c). **(g-i)** Simulated spectra under the same conditions of the experiment. **(j-l)** Convolution of (g-i) with a Gaussian profile of 7.5 meV FWHM introduced in order to facilitate comparison with experiment.

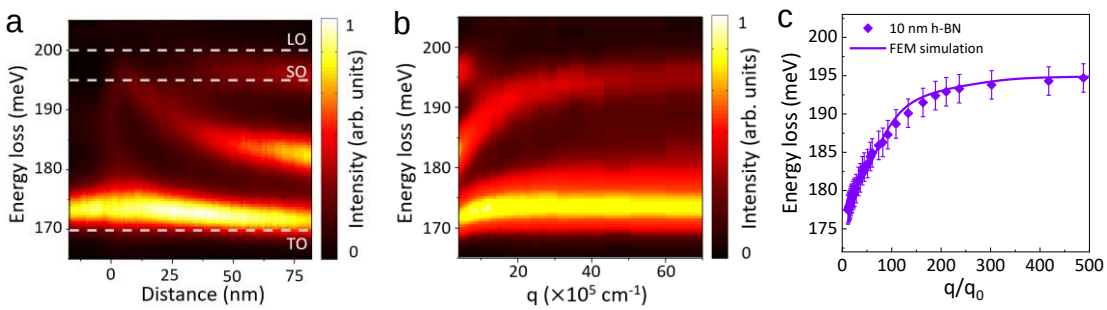

Supplementary Fig. 12. EELS dataset of a 10 nm thick h-BN flake. The step between adjacent spectra is 1 nm. **(a)** EELS spectra in real space and **(b)** in momentum space. In the latter, we use the relation $2q|d| + \phi_{\mathrm{refl}} = 2\pi$ to convert beam position d into momentum q. **(c)** Confinement calculated from the experimental data and that from FEM simulations. The error bars are the extraction deviation of EELS experiment data.

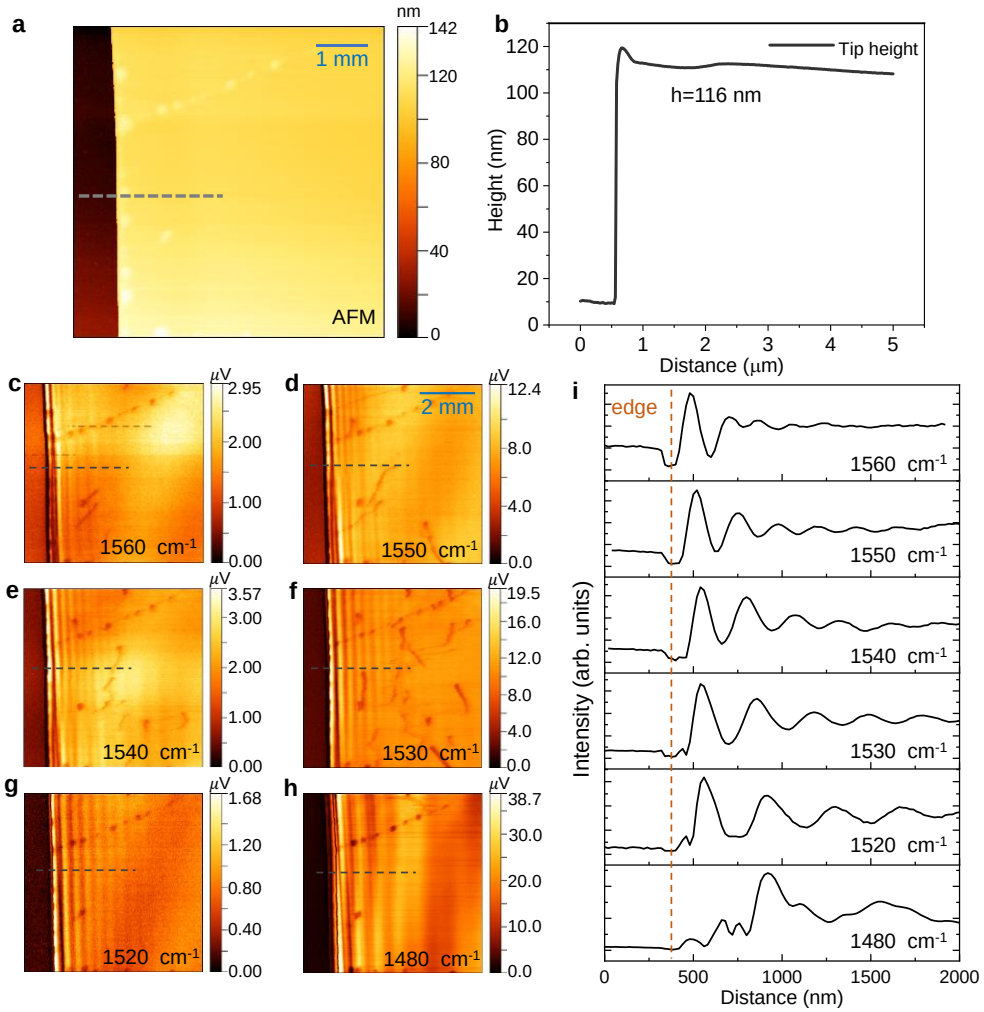

Supplementary Fig. 13. s-SNOM measurements of a 116 nm thick h-BN flake. **(a)** AFM image of the h-BN sample placed on a SiO_2 substrate. **(b)** Change in tip height along the dashed line in (a), indicating a thickness of 116 nm. **(c-h)** s-SNOM images at frequencies of 1560 cm^{-1} (193.5 meV), 1550 cm^{-1} (192.3 meV), 1540 cm^{-1} (191.1 meV), 1530 cm^{-1} (189.8 meV), 1520 cm^{-1} (188.6 meV) and 1480 cm^{-1} (183.6 meV), respectively. **(i)** Line profiles at different frequencies corresponding to (c-h) (see dashed lines there).

References

1 Kumar, A., Low, T., Fung, K. H., Avouris, P. & Fang, N. X. Tunable Light-Matter Interaction and the Role of Hyperbolicity in Graphene-hBN System. *Nano Lett.* **15**, 3172-3180 (2015).

2 Guo, X. *et al.* High-efficiency modulation of coupling between different polaritons in an in-plane graphene/hexagonal boron nitride heterostructure. *Nanoscale* **11**, 2703-2709 (2019).

3 Garc á de Abajo, F. J. Optical excitations in electron microscopy. *Rev. Mod. Phys.* **82**, 209-275 (2010).

4 Raza, S. *et al.* Extremely confined gap surface-plasmon modes excited by electrons. *Nat. Commun.* **5**, 4125 (2014).

5 Wiener, A. *et al.* Electron-energy loss study of nonlocal effects in connected plasmonic nanoprisms. *Acs Nano* **7**, 6287-6296 (2013).

6 Govyadinov, A. A. *et al.* Probing low-energy hyperbolic polaritons in van der Waals crystals with an electron microscope. *Nat. Commun.* **8**, 95 (2017).

7 Konecna, A. *et al.* Vibrational electron energy loss spectroscopy in truncated dielectric slabs. *Phys. Rev. B* **98**, 205409 (2018).

8 Kresse, G. & Furthmuller, J. Efficient iterative schemes for ab initio total-energy calculations using a plane-wave basis set. *Phys. Rev. B* **54**, 11169-11186 (1996).

9 Blochl, P. E. Projector Augmented-Wave Method. *Phys. Rev. B* **50**, 17953-17979 (1994).

10 Kresse, G. & Joubert, D. From ultrasoft pseudopotentials to the projector augmented-wave method. *Phys. Rev. B* **59**, 1758-1775 (1999).

11 Serrano, J. *et al.* Vibrational properties of hexagonal boron nitride: Inelastic X-ray scattering and ab initio calculations. *Phys. Rev. Lett.* **98**, 095503 (2007).

12 Kern, G., Kresse, G. & Hafner, J. Ab initio calculation of the lattice dynamics and phase diagram of boron nitride. *Phys. Rev. B* **59**, 8551-8559 (1999).

13 Cusco, R., Gil, B., Cassabois, G. & Artus, L. Temperature dependence of Raman-active phonons and anharmonic interactions in layered hexagonal BN. *Phys. Rev. B* **94**, 155435 (2016).

14 Garcıía de Abajo, F. J. Multiple excitation of confined graphene plasmons by single free electrons. *ACS nano* **7**, 11409-11419 (2013).

15 Rossouw, D. & Botton, G. A. Plasmonic Response of Bent Silver Nanowires for Nanophotonic Subwavelength Waveguiding. *Phys. Rev. Lett.* **110**, 066801 (2013).